Metal Oxide Transistors via Polyethylenimine Doping of the Channel Layer: Interplay of Doping, Microstructure, and Charge Transport

Wei Huang, Li Zeng, Xinge Yu, Peijun Guo, Binghao Wang, Qing Ma, Robert P. H. Chang, Junsheng Yu, Michael J. Bedzyk,* Tobin J. Marks,* and Antonio Facchetti**

Polymer doping of solution-processed In_2O_3 with small amounts of the electron-rich polymer, polyethylenimine (PEI), affords superior transistor performance, including higher electron mobility than that of the pristine In_2O_3 matrix. PEI doping of In_2O_3 films not only frustrates crystallization and controls the carrier concentration but, more importantly, acts as electron dopant and/or scattering center depending on the polymer doping concentration. The electron donating capacity of PEI combined with charge trapping and variation in the matrix film microstructure yields, for optimum PEI doping concentrations of 1.0%–1.5%, electron mobilities as high as ≈9 $cm^2 V^{-1} s^{-1}$ on a 300 nm SiO_2 gate dielectric, an excellent on/off ratio of ≈10^7, and an application optimal V_T. Importantly, these metrics exceed those of the pure In_2O_3 matrix with a maximum mobility ≈4 $cm^2 V^{-1} s^{-1}$. Furthermore, we show that this approach is extendible to other oxide compositions such as IZO and the technologically relevant IGZO. This work opens a new means to fabricate amorphous semiconductors via solution processing at low temperatures, while preserving or enhancing the mobility of the pristine polycrystalline semiconductor.

1. Introduction

Metal oxide (MO) based transistors are candidates for state-of-the-art flat panel display technologies and for next-generation electronics where high mobility and optical transparency in the visible region are required.[1–7] Furthermore, metal oxide semiconductor films can exhibit efficient charge transport in the amorphous state, essential to making them robust to mechanical stress when deposited on flexible substrates.[8–13] Currently, commercial metal oxide (semi) conductor films are primarily fabricated via vacuum vapor deposition processes such as sputtering, and are then patterned using expensive subtractive multistep photolithographic processes.[14–16] Another attraction of amorphous metal oxide transistors is the possibility of producing them in solution-based roll-to-roll fabrication processes.[17–27]

Indium oxide (In_2O_3) is among the most investigated oxide semiconductors, having a large band gap of more than 3.1 eV, a high intrinsic carrier concentration ($N \approx 10^{18}$ cm^{-3}), and large electron field-effect mobilities ($\mu \approx$ 10–50 $cm^2 V^{-1} s^{-1}$), thereby serving as an effective MO host matrix for several classes of high-performance TFT oxides.[28–33] Note, however, that the high N value raises the In_2O_3 Fermi level (E_F) very close to the conduction band minimum (CBM), thus limiting control over the film threshold voltage (V_T) and off-current (I_{off}).[9,34,35]

W. Huang, Dr. X. Yu, B. Wang, Prof. T. J. Marks, Prof. A. Facchetti
Department of Chemistry and the Materials Research Center
Northwestern University
2145, Sheridan Road, Evanston, IL 60208, USA
E-mail: t-marks@northwestern.edu; a-facchetti@northwestern.edu

W. Huang, Prof. J. Yu
State Key Laboratory of Electronic Thin Films and Integrated Devices
School of Optoelectronic Information
University of Electronic Science and Technology of China (UESTC)
Chengdu 610054, China
E-mail: jsyu@uestc.edu.cn

L. Zeng, Prof. M. J. Bedzyk
Applied Physics Program and the Materials Research Center
Northwestern University
2220 Campus Drive, Evanston, IL 60208, USA
E-mail: bedzyk@northwestern.edu

Dr. P. Guo, Prof. R. P. H. Chang
Department of Materials Science
and the Materials Research Center
Northwestern University
2220 Campus Drive, Evanston, IL 60208, USA

Dr. Q. Ma
DND-CAT Synchrotron Research Center APS/ANL Building
432A, 9700 S. Cass Ave., Argonne, IL 60439, USA

Prof. A. Facchetti
Polyera Corporation
8045 Lamon Avenue, Skokie, IL 60077, USA

DOI: 10.1002/adfm.201602069

© 2016 WILEY-VCH Verlag GmbH & Co. KGaA, Weinheim

Furthermore, In_2O_3 performs optimally in the polycrystalline state, limiting its applications in mechanically flexible electronics and large area fabrication.[36,37] The conventional strategy to stabilize In_2O_3-based amorphous phases is to introduce additional cations to form binary (e.g., In+Zn in IZO) and ternary (e.g., In+Zn+Ga in IGZO) amorphous films in both vapor and solution film growth.[38–40] To date, amorphous IGZO (indium–gallium–zinc oxide) is by far the optimal semiconductor for industrial electronic applications, with acceptable electron mobilities combined with low I_{off}, near-zero V_T, and stable $I–V$ characteristics.[8,41] For these reasons, strategies which lead to additional amorphous, high-mobility, and stable MO compositions are highly desirable.

We recently reported a new approach to amorphous metal oxides, e.g., In_2O_3, by chemically "doping" the film with the electrically insulating polymer poly(4-vinylphenol) (PVP), resulting in high-performance, transparent, and mechanically flexible amorphous TFTs.[35] However, the electron mobility (μ_e) of PVP-doped In_2O_3 TFTs on 300 nm SiO_2/Si gate dielectrics falls monotonically as the PVP concentration is increased, from ≈3 $cm^2 V^{-1} s^{-1}$ for the neat In_2O_3 matrix to ≈1.5–0.2 $cm^2 V^{-1} s^{-1}$ for 10–20 wt% PVP doping due to concomitant PVP charge trapping and film amorphorization. Optimal device performance, corresponding to an amorphous phase with an I_{on}/I_{off} of ≈10^6–10^7, a V_T of ≈1.2 V, and a $\mu_e \approx 2$ $cm^2 V^{-1} s^{-1}$, is obtained when ≈5 wt% PVP is admixed. Consequently, as in the case of doping In_2O_3 with light elements, high on/off ratios, proper V_T metrics, and stability are achieved by sacrificing the In_2O_3 matrix carrier mobility.

In this paper, we show for the first time that polymer doping of solution-processed metal oxides with polyethylenimine (PEI) significantly enhances transistor performance, including mobility, over the pristine MO matrix. Our data demonstrate that the mechanism by which PEI operates is very different from that of PVP, and a structurally similar polar polymer, poly(vinyl alcohol) (PVA), despite the fact that all these polymers are electrical insulators. PEI doping of In_2O_3 films not only frustrates crystallization and controls the carrier concentration but, more importantly, acts as electron dopant and/or scattering center depending on the polymer concentration. Thus, by carefully adjusting the polymer concentration (1.0%–1.5%), high mobility (maximum ≈9 $cm^2 V^{-1} s^{-1}$ on 300 nm SiO_2/Si) and excellent on/off ratios (≈10^7) are achieved, with performance exceeding that of the pure In_2O_3 matrix (maximum μ_e ≈4 $cm^2 V^{-1} s^{-1}$). Furthermore, this approach is applicable to other In_2O_3-based compositions such as IZO and IGZO.

2. Results and Discussion

2.1. Fabrication and Characterization of PEI-Doped In_2O_3 film

PEI (**Figure 1**a) is a commercially available polymer capable of efficient *n*-doping due to the electron-donor capacity of the tertiary amine groups. PEI contains one of the highest densities of amine groups among all known polymers and PEI electron-doping has been reported for several organic semiconductors, and is widely used in organic photovoltaic cells and transistors to enhance the charge transport of other organic materials.[42–46] Thus, intriguing questions arise as to whether PEI can be incorporated into inorganic oxides, whether it might intrinsically *n*-dope metal oxide semiconductor films, how this would affect film morphology and transport when this type of polymer is blended in MO films, and whether/how it differs from amine-free polymers.

Figure 1b illustrates the film and transistor fabrication process as well as the TFT structure used in this study. Briefly, TFTs are fabricated on doped Si substrates with 300 nm SiO_2 serving as the gate electrode and dielectric, respectively. The channel layer, consisting of an x wt% PEI-doped In_2O_3 blend, indicated here as In_2O_3:x% PEI; x = 0%–8%, was deposited by spin-coating aqueous PEI-In_2O_3 precursor solutions. Note that all films were fabricated using sol–gel chemistry formulations since PEI is incompatible with the solvent/fuel used in combustion synthesis as, for instance, in previous PVP doping experiments.[35] Next, the spin-coated films were annealed at 250 °C for 30 min, and this process was repeated three times to achieve the desired In_2O_3:x% PEI film thickness (see the Experimental Section for details). Finally, 40 nm thick Al source/drain electrodes were deposited by thermal evaporation through a shadow mask (channel length L = 100 µm, channel width W = 1 mm).

Before transport measurements, the film morphology and chemical composition of the In_2O_3:x% PEI films were characterized by AFM, SEM, UV–vis, XPS, FTIR spectroscopy, and grazing incidence X-ray diffraction (GIXRD). The AFM and SEM images (Figure 1c and Figure S1 (Supporting Information), respectively) indicate that the semiconducting films are all very smooth, with only slight increases in rms roughness from 0.33 (0% PEI) to 0.55 nm (6% PEI). The SEM images also suggest no obvious phase separation on PEI doping. The optical transmittance curves of the doped In_2O_3 films in Figure S2 (Supporting Information) show that PEI does not affect film transparency in the visible. GIXRD measurements (Figure 1d) indicate that the pristine In_2O_3 film is polycrystalline as evidenced by the very sharp, strong (222) reflection at $2\theta = 31.1°$ along with several weaker reflections at $2\theta = 22.1°$ (211), 36.0° (400), and 46.3° (431).[47] PEI doping of the In_2O_3 films strongly frustrates crystallization, especially for compositions with PEI >1%. After subtraction of the amorphous SiO_2 feature, the degree of In_2O_3:x% PEI blend crystallinity (χ_c) was estimated from the ratio of the area under the crystalline peaks to the total area under the X-ray diffraction pattern, fitting with a pseudo-Voigt function (Gaussian–Lorentzian product). Thus, the χ_c of neat In_2O_3 is ≈70% which decreases to ≈ 50% for 0.5% PEI doping. Importantly, χ_c dramatically falls to ≈ 9%, 7%, and 4% as the PEI doping increases to 1.5%, 3%, and 6%, respectively. Thus, In_2O_3:x% PEI films for x% > 1% are predominantly amorphous.

Next, XPS was utilized to better understand the overall chemical environment in the various In_2O_3:x% PEI compositions. The O1s spectra of all the films have similar peak shapes (Figure 1e, Figure S3 in the Supporting Information), which can be fitted with three individual components: (1) M–O–M lattice species at 529.8 ± 0.1 eV, (2) bulk and surface metal hydroxide (M–OH) species at 531.1 ± 0.1 eV, and (3) weakly bound M–OR species such as H_2O or CO_2 at 532.2 ± 0.1 eV (Table S1, Supporting Information).[48] Interestingly, as the PEI

© 2016 WILEY-VCH Verlag GmbH & Co. KGaA, Weinheim

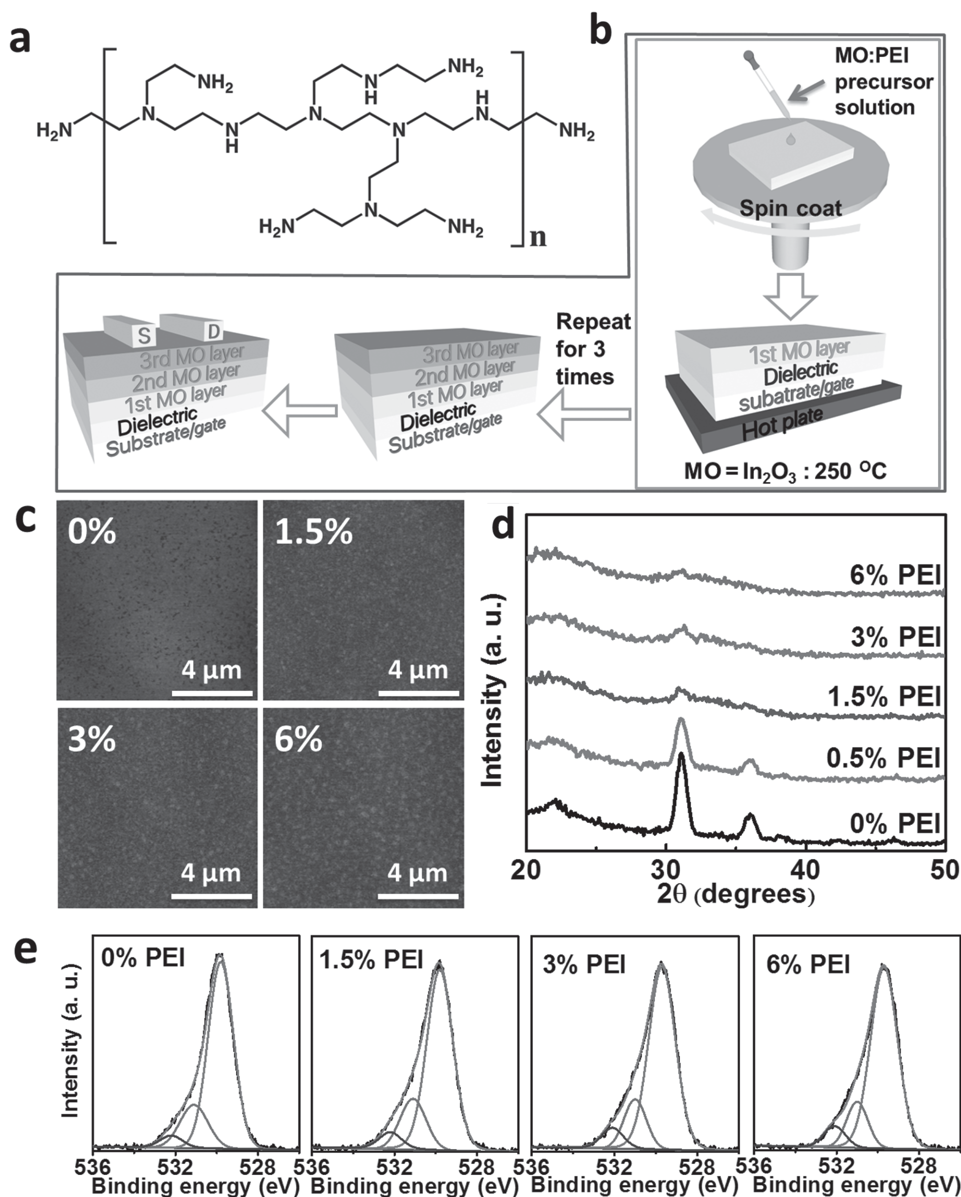

Figure 1. a) Chemical structure of PEI. b) Schematic of In_2O_3 film fabrication process and of the corresponding bottom gate top contact TFT structure used here. c) AFM images, d) GIXRD patterns, and e) O1s XPS of In_2O_3:x% PEI blend films with differing PEI concentrations.

concentration increases from 0% to 6%, the O contents of each species remains in the same range of 75%–76% for M–O–M, 17%–19% for M–OH, and 5%–8% for M–OR. Note that sufficient M–O–M lattice condensation is essential to achieve good charge transport in oxide semiconductors.[49,50] Importantly, the PEI-induced amorphous phases have essentially the same M–O–M lattice content (>70%) as the polycrystalline In_2O_3 precursor, arguing that the PEI doped In_2O_3 compositions should have high electron mobilities.

Since the PEI thermal decomposition onset begins at ≈250 °C,[51] XPS was also carried out to monitor blend film compositions for other elements. Figure S4 (Supporting Information) indicates that while the neat In_2O_3 films do not contain detectable amounts of C or N, PEI doping both at low (1.0%–1.5%) and high (6%) concentrations clearly produces detectable N 1s and C1s signals. Thus, even after the synthesis of In_2O_3 films and thermal annealing at 250 °C, the major elements of PEI are present in the films and not just as contaminants. However, both the C 1s and N 1s binding energies in the doped oxide films shift considerably versus pristine PEI. As shown in Figure S4 (Supporting Information), the PEI C 1s peak at 285.5 eV can be assigned to C—C and C—N bonds[52,53] whereas the additional peaks at 287.5 eV may be C=O groups arising from PEI hydrolysis and/or $C—NR_3^+$ groups arising from amine group quaternization.[51,54,55] The C 1s signal in these In_2O_3:PEI blends can also be fit to two peaks at ≈285.5 and ≈289.0 eV, the latter associable with C=O, $C—NR_3^+$ and more complex C—O bonded species.[55] Moreover, this peak intensifies as the PEI concentration increases, suggesting that PEI has significant reaction with O_2 during the annealing

© 2016 WILEY-VCH Verlag GmbH & Co. KGaA, Weinheim

process. The N 1s binding energies in PEI are assigned to C—N bonds (399.0 eV) and to strongly adsorbed CO_2 at surface amine centers (397.5 eV).[53] The N 1s ionization in the In_2O_3:*x*% PEI blends consists of two peaks located at 398.0–399.0 eV and at 403.0–404.0 eV, assignable to neutral N species partially coordinated to In cations[56,57] and/or to positively charged ammonium N atoms.[53,55] These results suggest that the PEI backbone remains within the film and that partial oxidation/quaternization/coordination occurs during annealing. FTIR spectroscopy also confirms the presence of substantial amounts of amine groups. Figure S5 (Supporting Information) shows the IR spectra of PEI and In_2O_3:PEI blend films. Amine modes at 1565 cm^{-1} (N—H bending) and 3200–3400 cm^{-1} (N—H stretching) are very strong in the pure PEI film, as are C—H bending at 1470 cm^{-1} and C—H stretching modes at 2825 and 2945 cm^{-1}.[58,59] While neat In_2O_3 exhibits only weak absorptions at 3300–3500 cm^{-1} due to absorbed water, the doped films clearly show amine signatures at ≈1565 and 3200–3400 cm^{-1}. These results indicate that, even after 250 °C annealing, substantial quantities of PEI amine groups remain intact. Furthermore, the doped MO films have C—H modes at 1470 cm^{-1} and a peak at ≈1630 cm^{-1} assignable to C═O and/or C═C arising from PEI decomposition products.[54]

2.2. Electrical Characteristics of Transistors Based on Polymer-In_2O_3 Blends

The transport characteristics of the In_2O_3:*x*% PEI TFTs measured in ambient reveal that PEI doping has a profound influence on TFT performance. **Figure 2** and Figures S6 and S7 (Supporting Information) show representative *I*–*V* plots, indicating that as the PEI wt% increases from 0% to 1.5%, I_{off} falls from ≈10^{-7} to ≈10^{-11} A, and then stabilizes at higher PEI wt% (≥1.5%). Interestingly, the TFT on-current (I_{on}) follows a different behavior than I_{off} and does not fall monotonically as the polymer dopant wt% increases, as previously reported for PVP doping (Figure S8, Supporting Information).[35] Thus, I_{on} increases from 1.54 ± 0.24 × 10^{-3} A (0% PEI) to 2.25 ± 0.27 × 10^{-3} A (0.5% PEI) to 2.96 ± 0.36 × 10^{-3} A (1% PEI). Next, the on-current begins to fall in the 1.5%–3% region (from 2.14 ± 0.29 × 10^{-3} A at 1.5% to 4.87 ± 0.22 × 10^{-4} A at 3%), then falls precipitously (≈10^{-5} A) for higher PEI content (> 4%). Simultaneously, the turn-on voltage shifts to a more positive values from −29 to −22 V for pristine In_2O_3 to −14 to −9 V for films with PEI contents of 1.0%–1.5% to ≥+2 V for larger PEI contents (>4%).

These combined changes in *I*–*V* data translate into major TFT transport parameter shifts (**Table 1**), extracted in saturation using conventional MOSFET equations.[9,35] Note that here we report the average of at least 10 TFT devices because in our arrays there are approximately 10 devices in the middle of the substrate. Only the TFTs outside the central part of the glass were excluded because of the film inhomogeneity at the edges of spin-coated films (a well-known phenomenon). Furthermore, several batches of 10 TFT arrays were produced and the performance is highly reproducible. Thus, the field-effect mobility of In_2O_3:*x*% PEI TFTs increases from ≈4.2 to >8 $cm^2\ V^{-1}\ s^{-1}$ when PEI increases from 0% to 1.0%–1.5%, then falls to ≈4 $cm^2\ V^{-1}\ s^{-1}$ at PEI concentrations of 2.0%–2.5% and further to ≤1 $cm^2\ V^{-1}\ s^{-1}$ at >6% PEI concentration. Concurrently, I_{on}/I_{off} abruptly increases from ≈10^4 (0% PEI) to

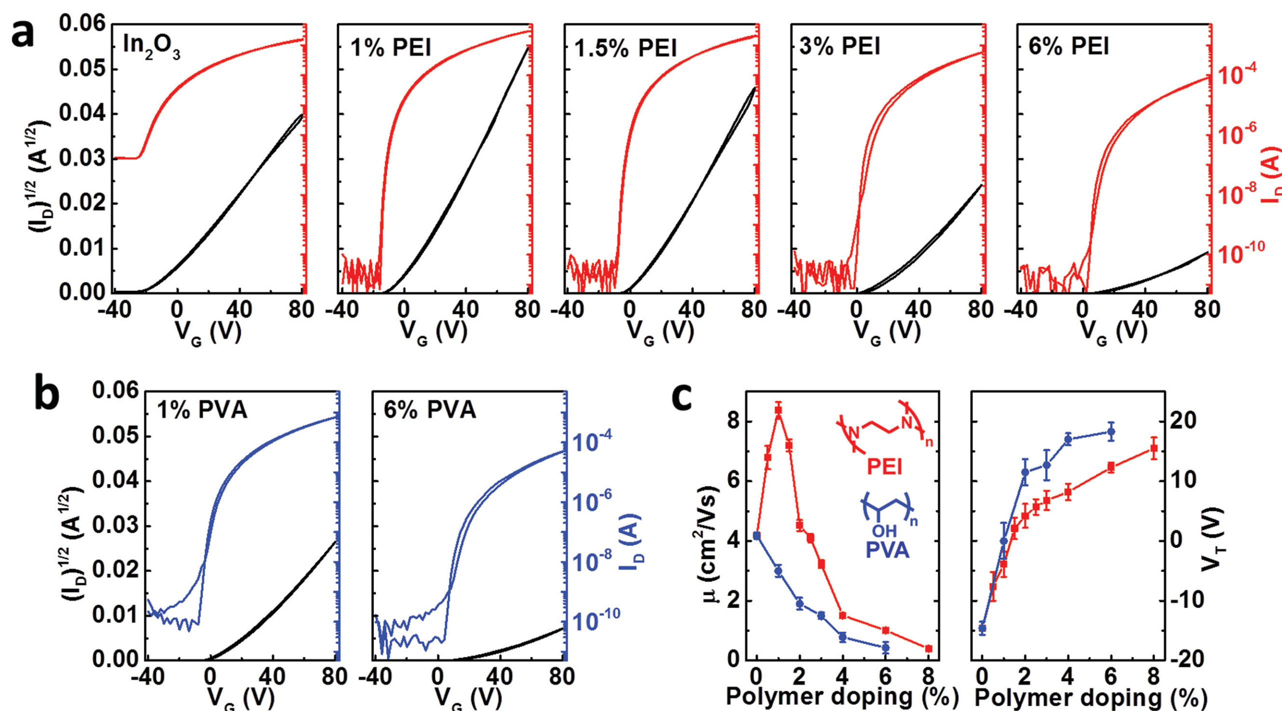

Figure 2. Representative transfer characteristics for the indicated a) In_2O_3:x% PEI and b) In_2O_3:x% PVA TFTs. V_D = +80 V. c) TFT mobility and threshold voltage for In_2O_3:x% PEI and In_2O_3:x% PVA films as a function of the polymer concentration.

© 2016 WILEY-VCH Verlag GmbH & Co. KGaA, Weinheim

Table 1. Performance metrics for In_2O_3:x% polymer TFTs with the indicated polymer concentrations.

TFT Metric[a)]	PEI concentration [%]									
	0	0.5	1	1.5	2	2.5	3	4	6	8
μ [cm^2 V^{-1} s^{-1}]	4.18 ± 0.11	6.78 ± 0.39	8.37 ± 0.28	7.20 ± 0.20	4.52 ± 0.18	4,10 ± 0.14	3.22 ± 0.13	1.51 ± 0.05	1.01 ± 0.02	0.40 ± 0.01
V_{th} [V]	−14.6 ± 1.1	−7.6 ± 2.4	−3.9 ± 2.1	2.1 ± 1.8	4.2 ± 2.0	5.7 ± 1.3	6.8 ± 1.6	8.2 ± 1.4	12.3 ± 0.8	15.5 ± 1.8
I_{on}/I_{off}	10^4	10^6	10^6–10^7	10^7	10^6–10^7	10^6–10^7	10^6–10^7	10^6–10^7	10^6	10^6

	PVA concentration [%]					
	0	1	2	3	4	6
μ [cm^2 V^{-1} s^{-1}]	4.18 ± 0.11	3.01 ± 0.21	1.93 ± 0.25	1.49 ± 0.19	0.78 ± 0.16	0.43 ± 0.19
V_{th} [V]	−14.6 ± 1.1	−1.5 ± 3.2	11.5 ± 2.2	12.7 ± 2.5	17.0 ± 1.0	18.3 ± 1.5
I_{on}/I_{off}	10^4	10^6–10^7	10^6–10^7	10^6	10^6	10^6

a)Each device is the average of a minimum of 10 devices.

≈10^6 (0.5% PEI), maximizes at ≈10^7 at 1.5% PEI, then remains at the same level (10^6–10^7) for the other compositions. Interestingly, V_{th} shifts to more positive values when the PEI concentration increases, reaching an optimal value of ≈0.0 V for PEI levels of 1.0%–1.5%. Note that all TFT data reported here are for devices fabricated on 300 nm SiO_2 gate dielectrics. Many studies have shown that high-*k* dielectrics enhance the mobility of metal oxide transistors,[18,60] and the reasons have been thoroughly discussed.[61,62] Thus, it is obvious that utilizing a high-*k* dielectric (e.g., Al_2O_3, ZrO_2) would further enhance the present transistor performance. Furthermore, bias stress tests on the present transistors indicate that PEI doping does not introduce severe TFT instability (Figure S9, Supporting Information).

Strikingly different behavior is observed for similarly processed PVA-based polymer-In_2O_3 blends where the TFT *I–V* characteristics (Figure 2 and Figure S10, Supporting Information) and device metrics (Table 1) follow trends similar to the previously reported PVP–MO formulations (processed there by combustion techniques).[30] Thus, for the In_2O_3:*x*% PVA TFTs, both I_{on} and FET mobility monolithically fall from 1.54 ± 0.24 × 10^{-3} (0% PVA) to 5.08 ± 0.22 × 10^{-5} A (6% PVA) and ≈ 4.2 (0% PVA) to ≈0.4 cm^2 V^{-1} s^{-1} (6% PVA), respectively. Moreover, the on/off ratio increases from 10^4 (0% PVA) to 10^6 (6% PVA) and V_T shifts from −14.6 (0% PVA) to 18.3 V (6% PVA). Clearly PEI doping has a unique influence on oxide TFT performance with the interplay of electron doping enhancing, and scattering/amorphization diminishing, TFT performance. Thus, the mechanism by which PEI operates is very different from that when In_2O_3 is doped with light elements such as Ga and Zn or an amine-free insulating polymers such as PVP (for combustion)[35] or PVA (for sol–gel), which is always accompanied by lower mobility for optimal I_{on}/I_{off} ratios and V_Ts are obtained (see Figure S11, Supporting Information).

To demonstrate that PEI can electrically dope MO films, to date unprecedented in oxide TFTs, In_2O_3 devices having a spin-coated PEI film on top of the completed device with different In_2O_3 thicknesses were fabricated and evaluated (**Figure 3**a–c). The *I–V* curves reveal that the PEI-coated In_2O_3 TFTs are heavily doped and cannot be turned off, demonstrating that electron transfer from the amine N groups to the MO lattice is efficient, similar to that observed for organic semiconductors.[42–46] Note that the electrical conductivity of PEI films spin-coated on TFT architectures without In_2O_3 is negligible, confirming the intrinsic insulating nature of this polymer (Figure 3d). Thus, In_2O_3 electron doping raises the carrier concentration, increasing both off- and on-currents, since in this planar heterojunction structure, PEI only increases the carrier density without significantly affecting the film microstructure.[43,44] However, this is not the case for the In_2O_3:*x*% PEI blends where the devices are based on a bulk, rather than planar-heterojunctions. As noted for the planar devices, PEI only enhances the carrier density by electron transfer without altering the MO microstructure. However, for bulk-heterojunction In_2O_3 TFTs with increasing PEI concentrations, charge transport should be affected in four ways: (1) *Charge transfer*: PEI enhances the carrier concentration, increasing both I_{on} and I_{off}. (2) *Charge scattering*: PEI introduces film contaminants, creating charge traps and depressing transport. (3) *Microstructure*: GIXRD experiments clearly reveal that the film amorphous fraction increases, which in principal could depress transport efficiency. (4) *Density*: The overall oxide volume fraction decreases, reducing the carrier density. Thus, as shown in Figure 2 and Figures S6 and S7 (Supporting Information), PEI doping invariably depresses the transistor I_{off}, however, for very small amounts of PEI, the electron mobility and I_{on} increase. This doping result suggests that small amounts of PEI create a delicate balance between electron transfer, prefilling of immobile electron traps, and morphology disruption. This model is supported by the XPS data showing that the PEI content does not affect the extent of blend M–O–M lattice densification, essential for effective electron transport.

2.3. Polymer-In_2O_3 Blend Microstructure and TFT Performance Enhancement

For the above reasons and to gain more insight into atomic scale structural variations within these primarily amorphous blends, EXAFS techniques were applied to further define changes in the local InO_x polyhedral on PEI introduction. For In_2O_3 powders, the three peaks at $R \leq 4$ Å correspond to the In—O (CN = 6; R_1 = 2.19 Å), In—In (CN = 6; R_2 = 3.35 Å), and In—In (CN = 6; R_1 = 3.82 Å) shells (CN = coordination number, R = distance). Since the EXAFS peak height is related to CN

© 2016 WILEY-VCH Verlag GmbH & Co. KGaA, Weinheim

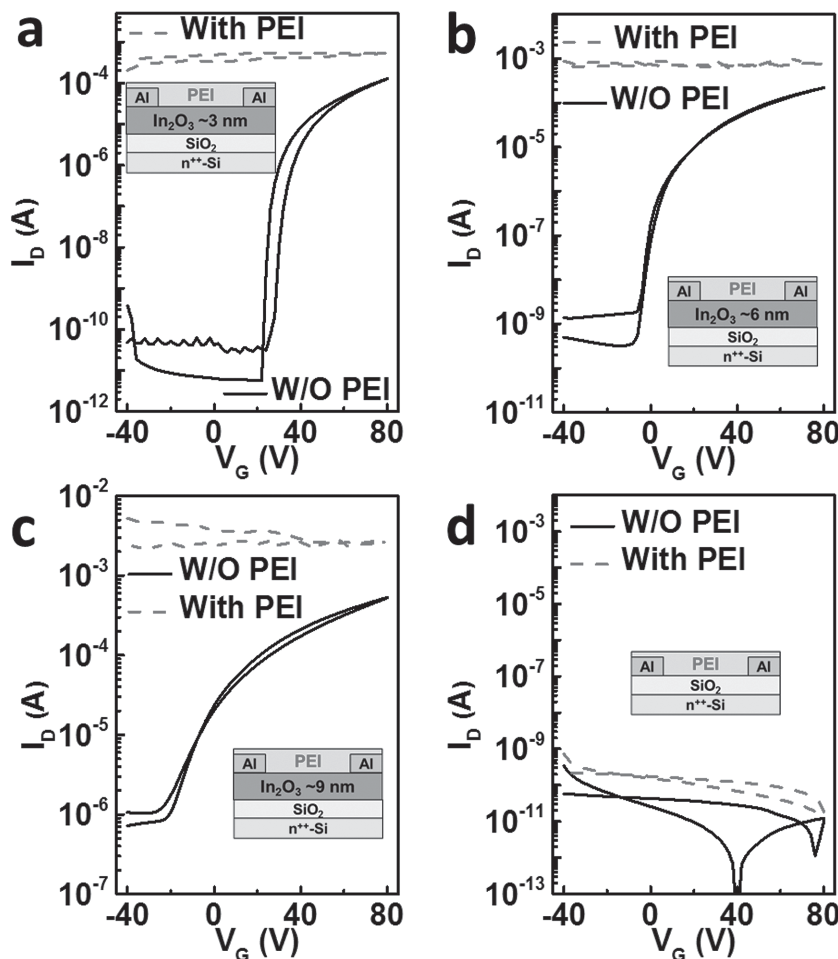

Figure 3. Transfer plots of In_2O_3 TFTs with/without PEI coated on the transistor with, a) ≈3 nm, b) ≈6 nm, and c) ≈9 nm In_2O_3 layer (insert: TFT structure). d) Transfer plots of PEI coated on electrical contacts fabricated on Si/SiO_x substrate (insert: TFT structure). V_D = +80 V.

while the peak position relates to interatomic distance, qualitative interpretation of the blend samples can be made by comparison to In_2O_3 powder. As shown in **Figure 4**a, on progressive PEI addition, the first shell CN remains relatively constant while the signatures of the second and third monotonically decline in intensity, indicating that these InO_6 CNs fall below 6. However, remarkably, even at 6% doping, a relatively strong third shell fringe is detected, which is rarely seen in amorphous oxide EXAFS.[35,63,64] Since completely amorphous materials lack a third shell, these data indicate that the heavily doped In_2O_3 films retain some degree of order.

Quantitative EXAFS data analysis next focused on the first two shells (In—O and In···In), and data were fitted in *R*-space with *k*-weight 2. An intrinsic loss factor (S^2_0 = 1.06) for fitting the In K edge was obtained by modeling In_2O_3 powder, and held fixed when fitting the film data. The results on bulk In_2O_3 powder, a pristine In_2O_3 film, and 1.5%, 3%, and 6% PEI doping are shown in Figure 4b,c, with data summarized in Table S2 (Supporting Information). The CNs of the first two shells of bulk In_2O_3 were both fixed at CN = 6 for reference. The first shell CN of all films remains close to 6, independent of the PEI doping level, meaning that the InO_6 octahedra remain relatively intact despite the PEI doping. Unlike the first shell, the CNs of the second shells are PEI content dependent, varying from 6 (powder) to 5.35 (0%) to 4.64 (1.5%) to 4.05 (6%), showing increased local disorder on PEI doping. This result is consistent with the TFT mobility trends for higher PEI contents, indicating that PEI disrupts lattice and electron conduction pathways. The derived bond lengths in both first and second shells do not vary significantly: 2.15–2.18 Å for first shell, and 3.37–3.38 Å for second shell. Overall, PEI doping disrupts lattice order, albeit to a lesser extent than PVP (see Figure S12, Supporting Information), leaving a sufficient density of connected InO_x polyhedra for efficient charge transport.[65]

X-ray reflectivity (XRR) was utilized to further examine film quality and structural evolution upon PEI doping and multilayer deposition, since it is sensitive to film electron density, layer spacing, and interfacial roughness (Figure 4d,e). Recall that the In_2O_3:*x*% PEI films are trilayers successively spun from the same precursor formulation. The average electron density of each film (Table S3, Supporting Information) is determined by integrating the electron density profile (Figure 4e) over the film region and extracting the slope of the integrated profile. Combined with thickness information, it can be seen that as the PEI content increases from 0% to 6%, the film thickness gradually increases from ≈9.8 to 12.3 nm, and the calculated average electron density decreases monotonically from ≈1.7 e $Å^{-3}$ (neat In_2O_3) to ≈1.6 e $Å^{-3}$ (1.5% PEI) to ≈1.4 e $Å^{-3}$ (6% PEI). Furthermore, the neat In_2O_3 film exhibits a relatively uniform electron density distribution throughout the film thickness (1.6–1.8 e $Å^{-3}$) despite the fact that the first, second, third layers are annealed at 250 °C for different times (90, 60, and 30 min, respectively—see the schematic in Figure 1b). However, the electron density distributions of the In_2O_3:*x*% PEI blends are not as uniform (Figure 4e). Thus, for the In_2O_3:1,5% PEI film, the electron densities of the second and third layers, 1.61 e $Å^{-3}$ (second layer) and 1.40 e $Å^{-3}$ (third layer), are lower than that of the first layer (1.69 e $Å^{-3}$). Note the XPS-derived M–O–M content for all films remains constant even though the film crystallinity decreases dramatically, indicating that the overall metal oxide formation remains efficient and the majority of electron density decrease most likely reflects structural relaxation and porosity formation in the second and third In_2O_3 layers. Thus, several aspects of transport in In_2O_3:*x*% PEI TFTs mimic that of bilayer metal oxide transistors,[34,66–68] where in the present case, the layer adjacent to the dielectric offers an efficient channel for charge transport, with low PEI content prefilling traps and minimally disturbing electrical continuity, and any successive layer(s) controlling conductance, resulting in low I_{off} and suitable V_T. In the devices with PEI doping, the second and third In_2O_3 layers, which have inferior density, control the

© 2016 WILEY-VCH Verlag GmbH & Co. KGaA, Weinheim

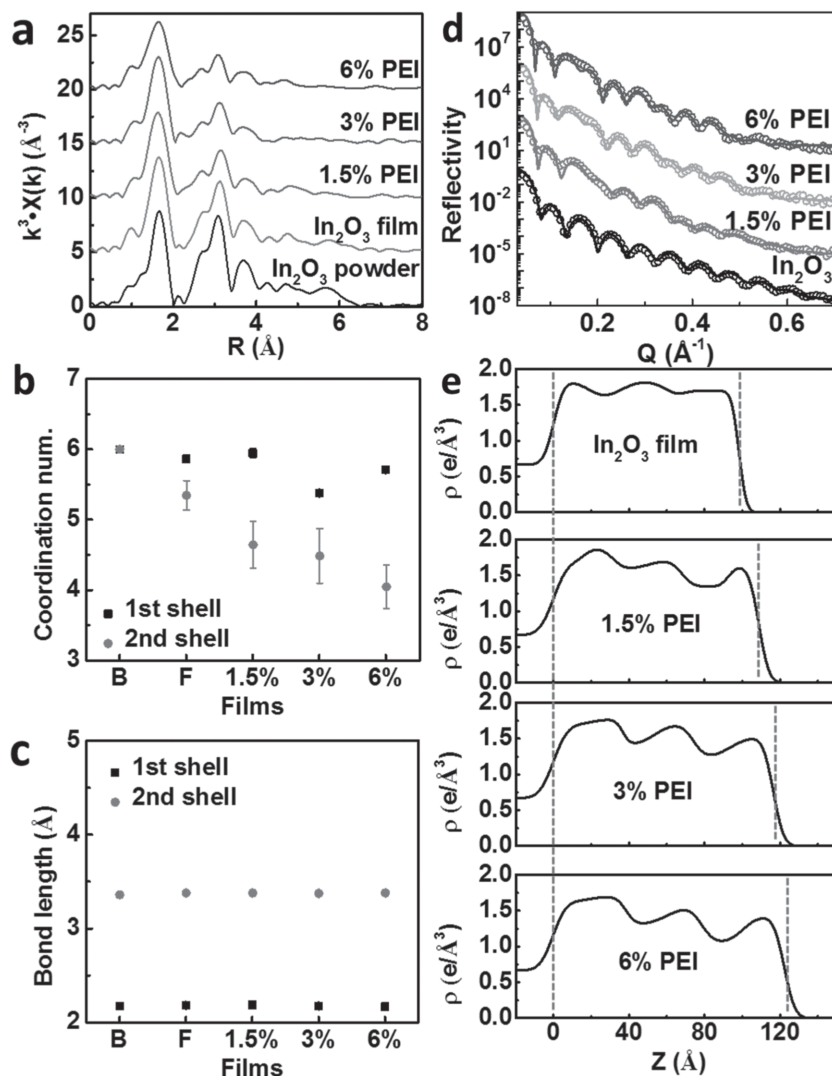

Figure 4. a) Comparison of the In K-edge *p*-RDFs of In_2O_3 powder, a neat In_2O_3 film, In_2O_3:x% PEI blend with 1.5%, 3%, and 6% PEI concentrations. b,c) Derived coordination number, In—O bond lengths for the indicated films. d) XRR plots and e) corresponding electron density profiles of the indicated In_2O_3:x% PEI blend films.

charge conductance and contribute to the low I_{off} and positively shifted V_T.

Meanwhile, the substantial M–O–M networks, as established by XPS and EXAFS, ensure efficient electron carrier transport. As shown in Figure S13 (Supporting Information), for In_2O_3 without PEI doping, extensive oxygen vacancies likely increase the carrier concentrations, resulting in a large I_{off} and negative V_T. For very small amounts of PEI (<1.0%), the polymer (1) creates additional deep trap states that the PEI-induced transferred electrons can fill, (2) efficiently alters the film microstructure by enhancing the amorphous portion as well as forming a complex multilayer-like structure characterized by a modulation of the film/electron density as shown in Figure 4e. This likely contributes to a reduced I_{off} and a V_T which shifts positively. For larger PEI contents of 1.0%–1.5%, the PEI transferred electrons are sufficient to fill all the deep traps and some of the shallow traps, resulting in enhanced I_{on} and field-effect mobility along with a depressed I_{off}. When the PEI content exceeds 1.5%, the large amounts of PEI disrupt the microstructure to a greater extent and create far more traps. Moreover, the overall MO volume fraction decreases as the PEI content increases. Consequently, the doping capacity of PEI is insufficient to overcome all other negative effects, thus depressing I_{on}, decreasing mobility, and continuously shifting the *I–V* characteristics to positive gate values.

Finally, in order to demonstrate the generality of the present PEI doping strategy, PEI-doped blends were investigated using IZO and IGZO as starting matrices. Our results again on a 300 nm SiO_2 gate dielectric indicate that PEI is equally effective in enhancing the FET mobilities of these materials, from 6.8 and 5.6 $cm^2\ V^{-1}\ s^{-1}$ (undoped) to 10.2 and 7.9 $cm^2\ V^{-1}\ s^{-1}$ (0.5% PEI doped) for IZO and IGZO, respectively (details in Supporting Information, Figure S14). Although microstructural investigations are still in progress for these materials, it is clear that PEI is equally effective at increasing mobility at low PEI doping levels.

3. Conclusions

In conclusion, a novel approach has been developed to enhance the performance of polymer-doped metal oxide semiconductors. Unlike previous inorganic or organic In_2O_3 doping methods, PEI doping not only effectively frustrates crystallization and controls the carrier concentration in the In_2O_3 channel, but also increases the electron mobility of the In_2O_3 matrix. The electron donating capacity of PEI combined with charge trapping and matrix film microstructure tuning, yields for appropriate PEI doping levels, high mobilities along with optimal I_{off} and V_T. This work demonstrates that polymer doping of metal oxides is broad in scope and opens a new means to fabricate amorphous semiconductors via solution processing at low temperatures, while preserving or enhancing the mobility in the pristine polycrystalline semiconductor. We believe that the concept demonstrated here for metal oxide transistors should be applicable to many opto-electronic devices where critical components are metal oxide films.

4. Experimental Section

Precursor Solutions: For the metal oxide precursor preparation, each metal nitrate salt (354.8 mg of $In(NO_3)_3 \cdot xH_2O$; 297.2 mg of $Zn(NO_3)_2 \cdot xH_2O$; 399.6 mg of $Ga(NO_3)_3 \cdot xH_2O$; all from Sigma-Aldrich, 99.999% trace metals basis) was dissolved in 10 mL high purity deionized water (DI water). After stirring for about 1 h, the precursor solutions were combined by micropipet to desired molar ratios (for IZO, In:Zn = 7:3; for

© 2016 WILEY-VCH Verlag GmbH & Co. KGaA, Weinheim

IGZO, In:Ga:Zn = 72.5:7.5:20) and stirred. PEI (Sigma-Aldrich, average $M_W \approx 25\,000$ by LS, average $M_n \approx 10\,000$ by GPC, branched) and PVA (Sigma-Aldrich, M_w 13 000–23 000, 87%–89% hydrolyzed) were also dissolved in DI water to achieve concentrations of 20 mg mL^{-1}. After these solutions were stirred for at least 6 h, the PEI or PVA solution was added to the matal oxide precursor solution to achieve the desired polymer weight fraction (In_2O_3:*x*% PEI; x = 0.5%–8%; In_2O_3:*x*% PVA; x = 1%–6%; IZO:*x*% PEI; x = 0.5%–6%; IGZO:*x*% PEI; x = 0.5%–6%). After addition, the MO:polymer precursor solutions were stirred for 8 h before use.

Transistor Fabrication and Electrical Characterization: n^{++}-Si wafers with 300 nm thermally grown SiO_2 were used as the gate electrode and dielectric layer. Before spin-coating, the substrates were cleaned ultrasonically in isopropyl alcohol and in an O_2 plasma. Then, the MO:polymer precursor solutions were spin-coated at 3000 rpm for 20 s, and then annealed on a hot plate at 250 °C (for In_2O_3:polymer) or 300 °C (for IZO:polymer and IGZO:polymer) for 30 min. This process was repeated three times to achieve the desired thickness, ≈10 nm for neat In_2O_3, and 10–13 nm for In_2O_3:*x*% polymer depending on the polymer content. Finally, 40 nm Al source drain electrodes were thermally evaporated to form a channel length of 100 µm, and channel width of 1000 µm. No postfabrication thermal annealing was carried out for our devices. TFT characterization was performed under ambient in the dark on a custom probe station using an Agilent 1500 semiconductor parameter analyzer. The electron mobility (μ) was calculated in the saturation region by the following equation

$$I_{DS} = \frac{WC_i}{2L}\mu(V_{GS} - V_T)^2 \tag{1}$$

Here C_i is the capacitance per unit area of the dielectric layer, V_T is the threshold voltage, and V_{GS} is gate voltage. W and L are channel width and length, respectively. Although the channels of these transistors are not patterned, the mobility measured here is accurate since the source/drain W/L ratio is within a range accepted by the community. Indeed, we achieve excellent on:off current ratios, eliminating the possibility of artifacts due to parasitic currents. Note that our goal here is not to achieve record mobilities but to make a direct comparison with previous work.

Oxide Film Characterization: AFM film topographies were imaged with a Veeco Demension Icon scanning Probe Microscope using tapping mode. SEM characterizations were carried out on a Hitachi SU8030 FE-SEM. GIXRD and XRR measurements were carried out with a Rigaku SmartLab Thin-film Diffraction Workstation using a high intensity 9 kW copper rotating anode X-ray source which is coupled to a multilayer optic. XPS was performed on Thermo Scientific ESCALAB 250Xi at a base pressure of 4.5×10^{-10} mbar (UHV). Spectra were obtained after the surface of the film was etched for about 2 nm to minimize surface contamination. FTIR spectra were collected by Nexus 870 spectrometer (Thermo Nicolet) with a single reflection horizontal ATR accessory having a diamond ATR crystal fixed at incident angle of 45°. XAFS experiments were conducted at the 5BM-D beamline at the Advanced Photon Source of Argonne National Laboratory (ANL). Samples were prepared by the procedure described above, but deposited on fused-quartz substrates (SPI Supplies) instead of Si ones. The incident X-ray was collimated to a 2 mm (horizontal) by 0.5 mm (vertical) beam size. The incident beam energies were tuned to near In K-edge (27940 eV) to measure EAXFS spectra for all PEI-doped films. Samples were placed at a grazing incident angle ($\alpha = 1.6°$) condition, and data were collected under fluorescence mode by putting two four-element silicon drift detectors (SII NanoTechnology) just above the samples' surfaces. The reference powders were uniformly spread on Scotch tape (3M Corp.) and measured through transmission mode by using ionization chamber (Oxford-Danfysik). The normalized linear EXAFS absorption coefficient $\chi(k)$ can be fit by

$$\chi(k) = S_0^2 \sum_i \frac{N_i f_i(k)}{kR_i^2} \exp\left(-\frac{2R_i}{\lambda(k)}\right) \times \exp\left(-2k^2\sigma_{R_i}^2\right)\sin(2kR_i + \delta(k)) \tag{2}$$

where S_0 is the intrinsic loss factor; $\lambda(k)$ is the electron mean free path; N_i and R_i are the coordination number (CN) and bond distance of the ith shell of the absorbing atom, respectively; $f_i(k)$ and $\delta_i(k)$ are the backscattering amplitude and the phase shift; and $\exp(-2k^2\sigma_{Ri}^2)$ is the Debye–Waller factor—a measure of the structural disorder or variation in R_i. The Fourier transformation of $\chi(k)$ generates a *pseudo*-radial distribution function (*p*-RDF) for the absorbing atom. For amorphous oxides, we are interested in how the coordination number, bond distances, and the Debye–Waller factors vary as a function of PEI doping concentration. EXAFS data were extracted and normalized by using ATHENA software packages.[69] The initial theoretical model was obtained by using FEFF simulations based on a cluster with the bixbyite structure of a 6 Å radius centered on the absorbing atom. All the normalized absorption coefficients $\chi(k)$ were then Fourier transformed using a Hanning window over the specified k-range to create the *p*-RDF plots which are shown in Figure 4a.

Supporting Information

Supporting Information is available from the Wiley Online Library or from the author.

Acknowledgements

The authors thank ONR (MURI N00014-11-1-0690), the Northwestern University MRSEC (NSF DMR-1121262), and Polyera Corp. for support of this research. This work made use of the J. B. Cohen X-Ray Diffraction Facility, EPIC facility, Keck-II facility, and SPID facility of the NUANCE Center at Northwestern University, which received support from the MRSEC program (NSF DMR-1121262); the International Institute for Nanotechnology (IIN); the Keck Foundation; and the State of Illinois. W.H. and B.H.W. thank the joint-PhD program supported by China Scholarship Council for fellowships. The EXAFS was performed at the DuPont-Northwestern-Dow Collaborative Access Team (DND-CAT) located at Sector 5 of the Advanced Photon Source (APS). DND-CAT is supported by E.I. DuPont de Nemours & Co., The Dow Chemical Company and Northwestern University. Use of the APS, an Office of Science User Facility operated for the U.S. Department of Energy (DOE) Office of Science by Argonne National Laboratory, was supported by the U.S. DOE under Contract No. DE-AC02-06CH11357.

Received: April 25, 2016
Revised: May 15, 2016
Published online: June 17, 2016

[1] J. Y. Kwon, J. K. Jeong, *Semicond. Sci. Technol.* **2015**, *30*, 024002.
[2] J. F. Wager, B. Yeh, R. L. Hoffman, D. A. Keszler, *Curr. Opin. Solid State Mater. Sci.* **2014**, *18*, 53.
[3] X. Yu, J. Smith, N. Zhou, L. Zeng, P. Guo, Y. Xia, A. Alvarez, S. Aghion, H. Lin, J. Yu, R. P. Chang, M. J. Bedzyk, R. Ferragut, T. J. Marks, A. Facchetti, *Proc. Natl. Acad. Sci. USA* **2015**, *112*, 3217.
[4] J. Tate, H. L. Ju, J. C. Moon, A. Zakutayev, A. P. Richard, J. Russell, D. H. McIntyre, *Phys. Rev. B* **2009**, *80*, 165206.
[5] V. Pecunia, K. Banger, H. Sirringhaus, *Adv. Electron. Mater.* **2015**, *1*, 1400024.
[6] J. G. Labram, Y.-H. Lin, K. Zhao, R. Li, S. R. Thomas, J. Semple, M. Androulidaki, L. Sygellou, M. McLachlan, E. Stratakis, A. Amassian, T. D. Anthopoulos, *Adv. Funct. Mater.* **2015**, *25*, 1727.
[7] G. Wang, Y. Mao, H. Wang, N. Persson, P.-H. Chu, N. Kleinhenz, B. Fu, M. Chang, N. Deb, M. A. Grover, E. Reichmanis, *ACS Nano* **2015**, *9*, 8220.
[8] K. Nomura, H. Ohta, A. Takagi, T. Kamiya, M. Hirano, H. Hosono, *Nature* **2004**, *432*, 488.

© 2016 WILEY-VCH Verlag GmbH & Co. KGaA, Weinheim

[9] E. Fortunato, P. Barquinha, R. Martins, *Adv. Mater.* **2012**, *24*, 2945.
[10] J. S. Park, W. J. Maeng, H. S. Kim, J. S. Park, *Thin Solid Films* **2012**, *520*, 1679.
[11] T. Rembert, C. Battaglia, A. Anders, A. Javey, *Adv. Mater.* **2015**, *27*, 6090.
[12] M. G. Kim, M. G. Kanatzidis, A. Facchetti, T. J. Marks, *Nat. Mater.* **2011**, *10*, 382.
[13] W. J. Lee, W. T. Park, S. Park, S. Sung, Y. Y. Noh, M. H. Yoon, *Adv. Mater.* **2015**, *27*, 5043.
[14] S. Lee, S. Jeon, R. Chaji, A. Nathan, *Proc. IEEE* **2015**, *103*, 644.
[15] A. Pierre, M. Sadeghi, M. M. Payne, A. Facchetti, J. E. Anthony, A. C. Arias, *Adv. Mater.* **2014**, *26*, 5722.
[16] S. S. Nkosi, I. Kortidis, D. E. Motaung, J. Keartland, E. Sideras-Haddad, A. Forbes, B. W. Mwakikunga, G. Kiriakidis, S. Sinha-Ray, *Appl. Surf. Sci.* **2013**, *280*, 79.
[17] K. K. Banger, Y. Yamashita, K. Mori, R. L. Peterson, T. Leedham, J. Rickard, H. Sirringhaus, *Nat. Mater.* **2011**, *10*, 45.
[18] Y. H. Kim, J. S. Heo, T. H. Kim, S. Park, M. H. Yoon, J. Kim, M. S. Oh, G. R. Yi, Y. Y. Noh, S. K. Park, *Nature* **2012**, *489*, 128.
[19] S. P. Schiessl, H. Faber, Y. H. Lin, S. Rossbauer, Q. Wang, K. Zhao, A. Amassian, J. Zaumseil, T. D. Anthopoulos, *Adv. Mater.* **2016**, *28*, 3952.
[20] A. Pierre, I. Deckman, P. B. Lechene, A. C. Arias, *Adv. Mater.* **2015**, *27*, 6411.
[21] D. E. Motaung, G. H. Mhlongo, I. Kortidis, S. S. Nkosi, G. F. Malgas, B. W. Mwakikunga, S. S. Ray, G. Kiriakidis, *Appl. Surf. Sci.* **2013**, *279*, 142.
[22] K. Jiang, A. Zakutayev, J. Stowers, M. D. Anderson, J. Tate, D. H. McIntyre, D. C. Johnson, D. A. Keszler, *Solid State Sci.* **2009**, *11*, 1692.
[23] J. Leppaniemi, O. H. Huttunen, H. Majumdar, A. Alastalo, *Adv. Mater.* **2015**, *27*, 7168.
[24] J. Jang, H. Kang, H. C. N. Chakravarthula, V. Subramanian, *Adv. Electron. Mater.* **2015**, *1*, 1500086.
[25] B. K. Sharma, B. Jang, J. E. Lee, S.-H. Bae, T. W. Kim, H.-J. Lee, J.-H. Kim, J.-H. Ahn, *Adv. Funct. Mater.* **2013**, *23*, 2024.
[26] C. H. Choi, L. Y. Lin, C. C. Cheng, C. h. Chang, *ECS J. Solid State Sci. Technol.* **2015**, *4*, P3044.
[27] S. H. Yu, B. J. Kim, M. S. Kang, S. H. Kim, J. H. Han, J. Y. Lee, J. H. Cho, *ACS Appl. Mater. Interfaces* **2013**, *5*, 9765.
[28] F. Fuchs, F. Bechstedt, *Phys. Rev. B* **2008**, *77*, 155107.
[29] H.-K. Noh, K. J. Chang, B. Ryu, W.-J. Lee, *Phys. Rev. B* **2011**, *84*, 115205.
[30] P. D. C. King, T. D. Veal, F. Fuchs, C. Y. Wang, D. J. Payne, A. Bourlange, H. Zhang, G. R. Bell, V. Cimalla, O. Ambacher, R. G. Egdell, F. Bechstedt, C. F. McConville, *Phys. Rev. B* **2009**, *79*, 205211.
[31] J. E. Medvedeva, R. Khanal, *Vacuum* **2015**, *114*, 142.
[32] W. Xu, H. Cao, L. Liang, J. B. Xu, *ACS Appl. Mater. Interfaces* **2015**, *7*, 14720.
[33] X. Yu, T. J. Marks, A. Facchetti, *Nat. Mater.* **2016**, *15*, 383.
[34] X. Yu, N. Zhou, J. Smith, H. Lin, K. Stallings, J. Yu, T. J. Marks, A. Facchetti, *ACS Appl. Mater. Interfaces* **2013**, *5*, 7983.
[35] X. Yu, L. Zeng, N. Zhou, P. Guo, F. Shi, D. B. Buchholz, Q. Ma, J. Yu, V. P. Dravid, R. P. Chang, M. Bedzyk, T. J. Marks, A. Facchetti, *Adv. Mater.* **2015**, *27*, 2390.
[36] M. Mativenga, D. Geng, B. Kim, J. Jang, *ACS Appl. Mater. Interfaces* **2015**, *7*, 1578.
[37] N. Zhou, D. B. Buchholz, G. Zhu, X. Yu, H. Lin, A. Facchetti, T. J. Marks, R. P. Chang, *Adv. Mater.* **2014**, *26*, 1098.
[38] J. W. Jo, J. Kim, K. T. Kim, J. G. Kang, M. G. Kim, K. H. Kim, H. Ko, Y. H. Kim, S. K. Park, *Adv. Mater.* **2015**, *27*, 1182.
[39] S. H. Jin, S. K. Kang, I. T. Cho, S. Y. Han, H. U. Chung, D. J. Lee, J. Shin, G. W. Baek, T. I. Kim, J. H. Lee, J. A. Rogers, *ACS Appl. Mater. Interfaces* **2015**, *7*, 8268.
[40] R. Khanal, D. B. Buchholz, R. P. H. Chang, J. E. Medvedeva, *Phys. Rev. B* **2015**, *91*, 205203.
[41] W. T. Park, I. Son, H. W. Park, K. B. Chung, Y. Xu, T. Lee, Y. Y. Noh, *ACS Appl. Mater. Interfaces* **2015**, *7*, 13289.
[42] H. C. Chen, S. W. Lin, J. M. Jiang, Y. W. Su, K. H. Wei, *ACS Appl. Mater. Interfaces* **2015**, *7*, 6273.
[43] M. Shim, A. Javey, N. W. S. Kam, H. Dai, *J. Am. Chem. Soc.* **2001**, *123*, 11512.
[44] Y. C. Du, H. Liu, A. T. Neal, M. W. Si, P. D. Ye, *IEEE Electron Device Lett.* **2013**, *34*, 1328.
[45] B. Sun, W. Hong, E. S. Thibau, H. Aziz, Z. H. Lu, Y. Li, *ACS Appl. Mater. Interfaces* **2015**, *7*, 18662.
[46] S. Fabiano, S. Braun, X. Liu, E. Weverberghs, P. Gerbaux, M. Fahlman, M. Berggren, X. Crispin, *Adv. Mater.* **2014**, *26*, 6000.
[47] H. Faber, Y. H. Lin, S. R. Thomas, K. Zhao, N. Pliatsikas, M. A. McLachlan, A. Amassian, P. A. Patsalas, T. D. Anthopoulos, *ACS Appl. Mater. Interfaces* **2015**, *7*, 782.
[48] G. H. Mhlongo, D. E. Motaung, I. Kortidis, N. R. Mathe, O. M. Ntwaeaborwa, H. C. Swart, B. W. Mwakikunga, S. S. Ray, G. Kiriakidis, *Mater. Chem. Phys.* **2015**, *162*, 628.
[49] Y. Hwan Hwang, J.-S. Seo, J. Moon Yun, H. Park, S. Yang, S.-H. Ko Park, B.-S. Bae, *NPG Asia Mater.* **2013**, *5*, e45.
[50] J. Socratous, K. K. Banger, Y. Vaynzof, A. Sadhanala, A. D. Brown, A. Sepe, U. Steiner, H. Sirringhaus, *Adv. Funct. Mater.* **2015**, *25*, 1873.
[51] V. V. Nedel'ko, B. L. Korsunskii, F. I. Dubovitskii, G. L. Gromova, *Polym. Sci. U.S.S.R.* **1975**, *17*, 1697.
[52] P. Louette, F. Bodino, J.-J. Pireaux, *Surf. Sci. Spectra* **2005**, *12*, 54.
[53] M. M. Khader, M. J. Al-Marri, S. Ali, G. Qi, E. P. Giannelis, *Am. J. Anal. Chem.* **2015**, *6*, 274.
[54] H. C. Haas, N. W. Schuler, R L. Macdonal, *J. Polym. Sci., Part A: Polym. Chem.* **1972**, *10*, 3143.
[55] O. Segut, G. Herlem, B. Lakard, V. Blondeau-Patissier, M. Nardin, S. Gree, J.-Y. Rauch, *Synth. Met.* **2010**, *160*, 1359.
[56] G. F. Zou, J. Zhao, H. M. Luo, T. M. McCleskey, A. K. Burrell, Q. X. Jia, *Chem. Soc. Rev.* **2013**, *42*, 439.
[57] Q. X. Jia, T. M. McCleskey, A. K. Burrell, Y. Lin, G. E. Collis, H. Wang, A. D. Li, S. R. Foltyn, *Nat. Mater.* **2004**, *3*, 529.
[58] W. Lu, M. Ling, M. Jia, P. Huang, C. Li, B. Yan, *Mol. Med. Rep.* **2014**, *9*, 1080.
[59] F. Wang, P. Liu, T. Nie, H. Wei, Z. Cui, *Int. J. Mol. Sci.* **2012**, *14*, 17.
[60] B. N. Pal, B. M. Dhar, K. C. See, H. E. Katz, *Nat. Mater.* **2009**, *8*, 898.
[61] E. Lee, J. Ko, K. H. Lim, K. Kim, S. Y. Park, J. M. Myoung, Y. S. Kim, *Adv. Funct. Mater.* **2014**, *24*, 4689.
[62] A. Zeumault, V. Subramanian, *Adv. Funct. Mater.* **2016**, *26*, 955.
[63] D. E. Proffit, Q. Ma, D. B. Buchholz, R. P. H. Chang, M. J. Bedzyk, T. O. Mason, N. J. Dudney, *J. Am. Ceram. Soc.* **2012**, *95*, 3657.
[64] D. B. Buchholz, Q. Ma, D. Alducin, A. Ponce, M. Jose-Yacaman, R. Khanal, J. E. Medvedeva, R. P. Chang, *Chem. Mater.* **2014**, *26*, 5401.
[65] J. Smith, L. Zeng, R. Khanal, K. Stallings, A. Facchetti, J. E. Medvedeva, M. J. Bedzyk, T. J. Marks, *Adv. Electron. Mater.* **2015**, *1*, 1500146.
[66] G. X. Liu, A. Liu, F. K. Shan, Y. Meng, B. C. Shin, E. Fortunato, R. Martins, *Appl. Phys. Lett.* **2014**, *105*, 113509.
[67] K. M. Kim, W. H. Jeong, D. L. Kim, Y. S. Rim, Y. Choi, M. K. Ryu, K. B. Park, H. J. Kim, *IEEE Electron Device Lett.* **2011**, *32*, 1242.
[68] W. H. Jeong, K. M. Kim, D. L. Kim, Y. S. Rim, H. J. Kim, *IEEE Trans. Electron Devices* **2012**, *59*, 2149.
[69] B. Ravel, M. Newville, *J. Synchrotron Radiat.* **2005**, *12*, 537.

© 2016 WILEY-VCH Verlag GmbH & Co. KGaA, Weinheim